In-line monitoring of the material extrusion additive manufacturing process by non-destructive methodologies

FORSTER, Rosanna, SOULIOTI, Dimitra, FETEIRA, Antonio <http://orcid.org/0000-0001-8151-7009>, GRAMMATIKOS, Sotirios and KORDATOS, Evangelos <http://orcid.org/0000-0002-5448-3883>

The International Journal of Advanced Manufacturing Technology
https://doi.org/10.1007/s00170-026-19170-7

ORIGINAL ARTICLE

In-line monitoring of the material extrusion additive manufacturing process by non-destructive methodologies

Rosanna Forster[1] · Dimitra Soulioti[1] · Antonio Feteira[1] · Sotirios Grammatikos[2] · Evangelos Kordatos[1]

Received: 7 March 2026 / Accepted: 15 September 2026

Abstract
This work involves the monitoring of the Material Extrusion (MEX) additive manufacturing process (also known as Fused Filament Fabrication, FFF) for polymeric materials through the combined application of Infrared Thermography (IrT) and Acoustic Emission (AE) methodologies. An innovative methodology has been developed for in-line monitoring of the additive manufacturing (AM) process, enabling the early identification of process-induced defects and manufacturing anomalies in additively manufactured polylactic acid (PLA) parts. The thermal distribution during material solidification and the acoustic activity of the additive manufacturing machine deposition system were recorded concurrently during the build and directly correlated with the resulting part quality. X-ray micro-computed tomography (micro-CT) was employed to benchmark the in-line monitoring results with respect to internal material defects. Furthermore, the mechanical behaviour of the additively manufactured parts was evaluated to establish a relationship between additive manufacturing process quality and structural integrity. The findings demonstrate that the developed in-line monitoring methodology enables the early detection of defects, which in turn can lead to improved additive manufacturing quality and enhanced mechanical performance of additively manufactured parts.

Keywords In-line monitoring · Additive manufacturing · Non-destructive evaluation · Infrared thermography · Acoustic emission · Micro-computed tomography

1 Introduction

Additive manufacturing is a rapidly growing and developing area of technology based on the successive application of material to create a physical 3D model with a near-net shape from a computer design [1]. This technology allows for a greater range of dimensional flexibility, low waste, greater material and resource efficiency and lower production costs compared to traditional manufacturing [2, 3]. Polymer based AM is on the forefront of development with applications across multiple sectors including construction, biomedical, automotive, aerospace and architecture [4]. The most used AM technique for additively manufactured polymeric materials is fused filament fabrication (FFF) [5] which is an extrusion and deposition-based process, where parts are built in a layer-by-layer sequence. The quality of the process can depend on the parameters of the process itself, and the material being built. Those parameters can affect also the surface quality and have been widely researched by several researchers [6–8]. Parameters such as layer height, printing and infill temperature [9], nozzle head temperature [10, 11], printing speed, raster angle, printing orientation [12] and nozzle size can affect the properties of the material and build part [13, 14] especially if the actual parameters vary from the expected. It has been widely reported in literature that poor selection of process parameters can lead to defects and failures [15–17]. There are several forms of defects which can be formed in this process including porosity, cracks, voids [18] and parts can have highly anisotropic properties which can be a disadvantage dependent on application. The creation and presence of these defects can be hard to detect during the manufacturing process hindered

✉ Evangelos Kordatos
e.kordatos@shu.ac.uk

1 School of Engineering and Built Environment, Sheffield Hallam University, Howard Street, Sheffield S1 1WB, UK

2 ASEMlab – Laboratory of Advanced and Sustainable Engineering Materials, Department of Manufacturing and Civil Engineering, Norwegian University of Science and Technology, Gjøvik 2815, Norway

Published online: 19 September 2026

further by the restriction on most AM equipment where once the process has started, if interrupted, it must be abandoned and restarted. These defects can be introduced into the manufactured part from multiple sources including porosity or inclusions in the filament, uneven layer deposition, uneven thermal distribution and nozzle clogging. Early detection of defects, such as excess vibration of the extruder head causing the head to divert from its path, can be detected by some FFF machines, but the technology isn't consistently reliable and cannot detect smaller defects such as voids or porosity in the AM samples [18].

In material extrusion of continuous fibre composites, hybrid reinforcement configurations have been shown to improve impact energy absorption and reduce damage severity, underscoring the role of reinforcement architecture in resisting dynamic loading [19]. In LPBF lattices, defect-aware optimisation frameworks that integrate micro-CT-derived porosity and strut-deviation information have delivered marked increases in specific energy absorption and compressive strength [20], and subsequent work has coupled defect mapping directly with geometric refinement to enhance mechanical performance [21]. These advances motivate robust in-line defect sensing to link process signatures with part integrity.

The application of non-destructive evaluation (NDE) techniques has been attempted to locate defects in conventionally manufactured polymeric materials and has been proven challenging [18] however, there has been progress when applied for the monitoring of the FFF process and inspection of build parts [22]. The application of X-ray based NDE techniques has seen success and has been proven capable to identify air-gaps or defects, down to the size of 1 µm. Chen et al. [23] scanned an ULTEM® (polyetherimide) AM prepared polymer sample using nano-computed tomography and presented a method to characterise the structural voids and air bubbles with regards to the build quality. This was successful with quantitively characterising the structural voids and air bubbles (diameter of 50–300 µm) in the sample and, when building with a default solid fill setting, found the part was only 88.9% filled. Kio et al. [24] presented a method using two X-ray interferometry techniques finding voids and cracks of printed sample of PLA and ABS supported with SEM imaging. It was reported that stepped-grating X-ray interferometry allowed for examination of an entire test object with a large field of view and single-shot X-ray interferometry has the potential for real-time in situ monitoring of the printing process within 1 mm of the printhead. Zekavat et al. [25] used X-ray CT to determine the differences in geometry and porosity analysis across PLA specimen with fabrication temperatures ranging 180–260 °C successfully. Through the use of X-ray CT, it was determined that samples manufactured within the manufacturers recommended range do not achieve 100% infill with a homogenous internal structure. Kattinger et al. [26] presented a method of in-situ X-ray CT studying the flow and melt behaviour of a modified polystyrene within a conventional nozzle. Multiple experiments were conducted relating to the heating temperatures (205–260 °C), filament speed (0.5 mm/s − 4.0 mm/s), extruder forces and air gaps between the filament and nozzle wall. It was concluded that the findings could aid future nozzle design and could serve a tool for future validation of numerical simulations. Meshkizadeh et al. [27] utilised a lesser used technique in thermography, specifically Thermal Signal Reconstruction and K-clustering to detect defects automatically in PLA printed samples. This allowed for the detection of artificial defects of varying size and depth to be detected.

In-line monitoring of the MEX process can deliver information which falls into two overarching categories, the monitoring of the AM system's health condition and the analysis of the manufactured product itself. Fu et al. [4] presented a review discussing the progress for the in-situ monitoring of the FFF process. It was established that, although there had been great progress in the field of in-situ monitoring of FFF for the detection of possible faults and abnormalities, more research is needed into how to apply this information to advance the technology in industrial settings. It was found that sensing systems such as vibration or acoustic emission are useful to localise where a system experiences a fault, however there is difficulty linking this information to specific fault sources due to the variation and "uniqueness" in the signals. Wu et al. [15] presented a data-driven methodology for the application of AE to the typical FFF process. AE signals from both a "normal" and "failed" print of the first printed layer of ABS were extracted and analysed. The failed builds were artificially induced by increasing the distance between the nozzle and build platform, therefore lessening the build platform adhesion. It was concluded that it is feasible to use this method for failure diagnosis including both identification and detection. Olowe et al. [28] used seven audio features in time and frequency space during FFF process to present a framework for AM quality prediction. This was combined with machine learning (ML) and advanced digital signal processing and concluded there was feasibility of using acoustic data for quality prediction and control in AM. It was also found that acoustic sensing can be valuable for real-time monitoring and quality control. In-situ/online monitoring of other additive manufacturing methodologies including direct laser metal deposition (LMD-DED) [29] and direct energy deposition (DED) [30] has been attempted with some success.

Thermography has also been used within an in-line monitoring capacity. AbouelNour et al. [31] presented a methodology of IrT and optical imagining used simultaneously to detect embedded defects in AM samples. It was concluded that this combination method could detect defects through temperature variations compared to a standard baseline, and there was a positive correlation between global hotspot temperature and the total number of embedded defects. Bauriedel et al. [32] used a combination of IrT and ML to forecast the mechanical properties of PLA parts. It was concluded, and validated through ML, that IrT temperature readings could accurately predict tensile strength of additively manufactured components without the need for additional hardware. Although the application of individual methods of NDE has been explored, more research is needed for the application of a combination of NDE methods and for the in-line monitoring of the printing process. AbouelNour et al. [33] presented a review of in-situ monitoring of sub-surface defects in AM and concluded that by integrating image and acoustic signal processing methods into the manufacturing and monitoring process, real-time feedback control of the process is plausible. IrT cameras were found to show sub-surface defects with sizes up to 1000 µm, and AE sensors used to record acoustic signals during the process could be analysed to provide information about the formation of internal defects. Both methods have been used separately in combination with ML algorithms.

In this study, an innovative in-line monitoring methodology for the MEX additive manufacturing process was developed, focusing on part quality across a range of process parameter settings using multiple NDE techniques, benchmarked against micro-computed tomography scans. The proposed in-line process monitoring approach, based on infrared thermography and acoustic emission, proved to be an effective tool for the early detection of defects during the build cycle, which can support additive manufacturing part quality assessment by providing insight into the outcome of the additive manufacturing process. Furthermore, the mechanical behaviour of the parts was evaluated to assess the relationship between process parameters and mechanical properties, reinforcing the significance of in-line monitoring for enhancing process stability and part quality. Although AE and IrT have been previously applied as standalone techniques, to the authors' knowledge, this is the first study combining IrT and AE for comprehensive in-line monitoring of a material extrusion additive manufacturing process under varied process parameter conditions.

2 Materials and methods

2.1 Additive manufacturing process

Terminology and vocabulary of this work conform with the BS EN ISO/ASTM 52900:2021 [1]. The test specimens were fabricated using an additive manufacturing system based on the material extrusion process category, specifically an Ultimaker S5 Pro Bundle (Utrecht, Netherlands). Fabrication was conducted within a temperature-controlled build environment, and the polymeric feedstock was stored and supplied via an integrated material handling system to ensure controlled material conditioning. Cooling during the build cycle was regulated by the machine's ventilation system, and system set-up and calibration were performed prior to each production run. Material deposition was carried out through a nozzle with a nominal orifice diameter of 0.4 mm. The build platform temperature was maintained at 60 °C, and an adhesive interface layer (PVA-based) was applied to the build surface to enhance part adhesion during the initial layers. The feedstock material was a transparent PLA, supplied as a continuous polymer strand with a nominal diameter of 2.85 mm ± 0.1 mm. PLA is a semi-crystalline thermoplastic polymer widely used in material extrusion additive manufacturing due to its low cost, relatively low melting temperature, good mechanical properties [34], and biocompatibility [35].

For the purposes of this study, both cubic specimens and standard tensile test specimens were produced, with each geometry manufactured in sets of three parts per production run. The cubic specimens are $10 \times 10 \times 10$ mm with a 7 mm brim to improve build platform adhesion. The material deposition strategy and toolpath for the cubic and tensile specimens are illustrated in Fig. 1. The tensile specimens' build orientation is XY as shown in Fig. 1b. The red "outer" wall is built first followed by the green "inner" wall. The diagonal infill is represented by the orange with the grey representing previous layers of deposited material. The tensile test samples were Dogbone 1 A fabricated according to BS EN ISO 527-1:2019 [36] and were built in sets of three, with the extrusion path shown in Fig. 1b and samples in Fig. 1d. The STL files were sliced in Ultimaker Cura 5.0.0 which includes five predefined process parameter sets (*Extra Fast*, *Fast*, *Normal*, *Fine* and *Extra Fine*) and the ability to create *Custom* process parameter set.

The applied process parameters for each parameters set are presented in Table 1. The present study is designed as a comparative assessment of predefined process parameter profiles rather than a strict single-parameter investigation, as multiple interdependent parameters vary simultaneously across the selected profiles. The cooling fan settings were kept the same at 100% speed across all process parameter sets. The *Custom* process parameter set was created from the *Extra Fine* predefined parameter set, with only the layer thickness (appears as layer height in the software process settings) changing. As shown in literature, it has a significant effect on the manufacturing quality, dimensional accuracy [37] and mechanical properties of extruded parts [38,

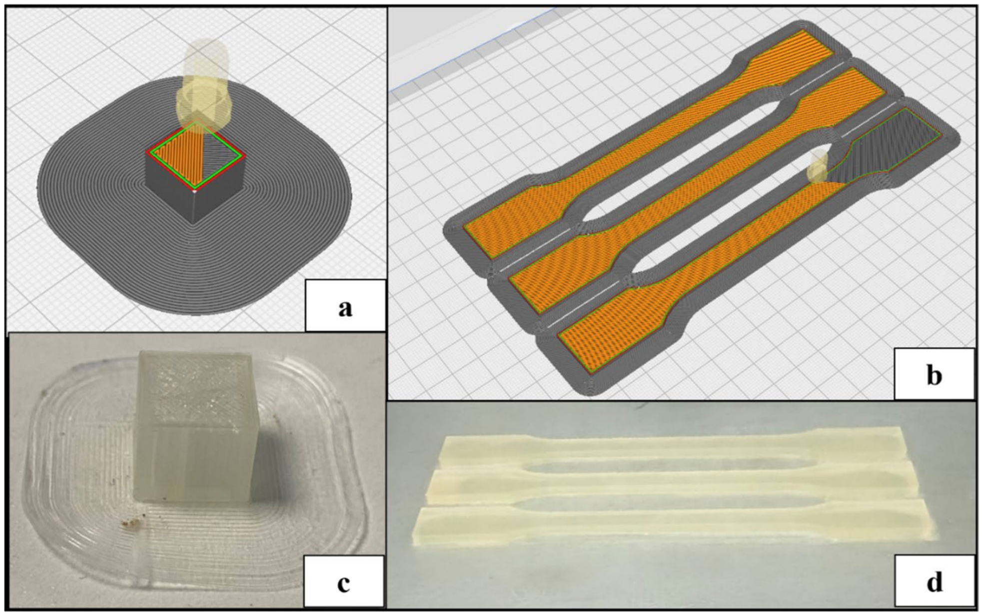

Fig. 1 Material deposition strategy and toolpath for the cubic and tensile specimens

Table 1 Process parameters for all samples

	Extra Fast	Fast	Normal	Fine	Extra Fine	Custom
Layer Thickness (mm)	0.30	0.20	0.15	0.10	0.06	0.04
Initial Layer Thickness (mm)	0.27	0.20	0.20	0.20	0.20	0.20
Line Width (mm)	0.40	0.40	0.40	0.40	0.40	0.40
Wall Thickness (mm)	0.80	0.80	0.80	0.80	0.80	0.80
Top/Bottom Thickness (mm)	0.90	0.80	1.00	1.00	1.00	1.00
Infill Density (%)	100.00	100.00	100.00	100.00	100.00	100.00
Infill Layer Thickness (mm)	0.30	0.20	0.15	0.10	0.06	0.04
Extrusion (printing) Temperature (°C)	210	205	200	200	195	195
Build platform temperature (°C)	60	60	60	60	60	60
Build (print) Speed (mm/s)	50	70	70	70	50	50
Infill Speed (mm/s)	50	70	70	70	50	50
Wall Speed (mm/s)	50	55	45	30	35	35
Cube build cycle time (mins)	4	7	10	15	24	32
Tensile sample build cycle time	2 h 20 min	2 h 49 min	4 h 2 min	6 h 14 min	9 h 40 min	14 h 7 min
Nominal volumetric deposition rate, mm³/s	6.0	5.6	4.2	2.8	1.2	0.8

39]. In beam-based additive manufacturing processes, volumetric energy density is often used to compare processing conditions. For the present material extrusion process, a true volumetric energy density was not calculated because the effective thermal power transferred from the heated nozzle to the polymer was not directly measured. Instead, the process intensity was assessed using the nominal volumetric deposition rate [40], $Q_v = vwh$, where v is the build speed, w is the line width and h is the layer thickness. This metric provides a comparative indication of material throughput across the process parameter sets.

2.2 In-line monitoring

The experimental setup of the in-line monitoring can be observed in Fig. 2. The extruded specimens were monitored by a FLIR IrT camera (X6540sc, Teledyne FLIR LLC, Portland, USA) with a capturing frame rate of 100 Hz and 640 × 512 pixels resolution, a noise equivalent temperature difference (NETD) of > 25 mK and a cooled indium antimonide (InSb) detector. The focal length was 50 mm and the field of view (FOV) was 11°x8.8° applying a sub window as ROI with 0.2 mm/pixel and PLA's emissivity value was 0.92 [41]. The camera was connected to a laptop which was recording the output data.

The AE data was captured by MISTRAS Micro-II express digital AE equipment (Micro-II Express, MISTRAS Group Inc, NJ, USA) with a wideband AE sensor with a frequency range of 100–900 kHz attached to the extrusion head using tape in accordance with the ASTM E650/E650M [42] standard. The characteristics of amplitude and cumulative hits were recorded during the manufacturing process

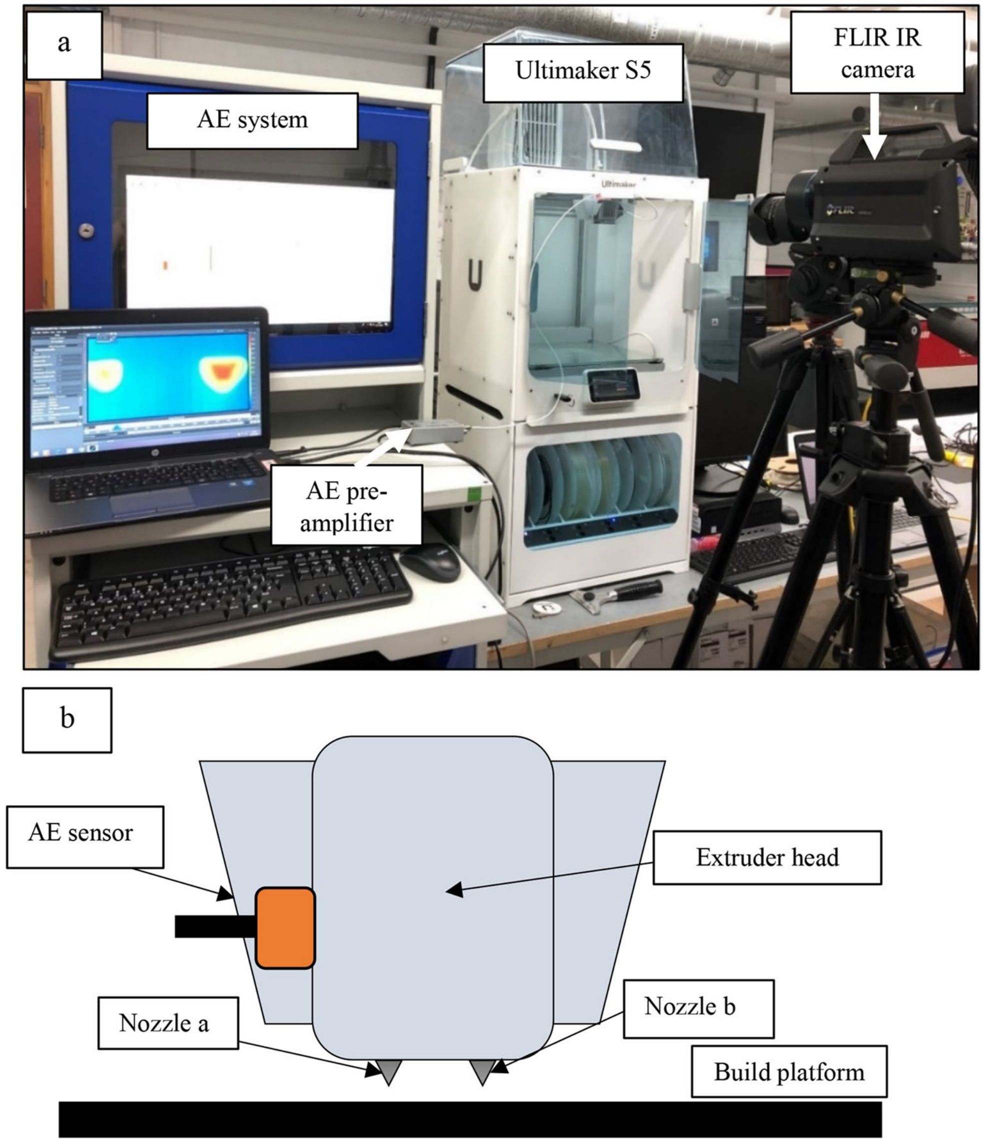

Fig. 2 (**a**) Experimental setup for the in-line monitoring process; (**b**) setup of the AE sensor on the extruder head

and to enhance the AE signals, a 40 db preamplifier (2/4/6) was selected. To ensure acoustic coupling, ANAGEL ultrasound gel was applied between the sensor and the extrusion head surface. The data was analysed in AEWin software.

2.3 Offline assessment

Micro-computed tomography was performed on Bruker Skyscan 1272 equipment (Bruker Corporation, MA, USA). The cubed specimens were placed on a raised surface, fixed in place with dental wax and rotated, with images taken layer by layer. The test selected used a source voltage of 55 kV, a source current of 160 µA and a theoretical resolution of 9 µm. The beam was filtered using an 0.5 mm Al filter and the elevation of the samples were 11 mm. The cubed specimens were scanned about 180° with a 0.7° step and the pixels were 2016×1344. The samples were stacked and secured in batches of 3 and scanned sequentially. The images were reconstructed in the NRecon software using GPUReconServer to remove artifacts from the reconstruction. Beam hardening correction of 20% was applied with a ring artifact correction of 9 and a smoothing value of 1. The images were aligned using DataViewer then rendered as a volume render in CTVox Bruker software. The reconstructed images were post-processed in CTAn Bruker software and rendered as a volume in CTVol Bruker software to determine porosity content.

2.3.1 CT analysis

The reconstructed files from NRecon were imported into CTAn, where a rectangular region of interest (ROI) was applied to remove the air surrounding the cubes during the scanning from the analysis. A range from image layer 400

(3.6 mm) and 700 (6.3 mm) was selected as a comparable data set and an optimal threshold was set. The lower bound of this threshold was 40 across all samples with the upper bound being the default 255. A custom processing task list was then applied to allow for 3D analysis and quantification of porosity provided as within Online Resource 1 (supplementary material). For each process parameter condition, one representative cubic specimen was selected for quantitative micro-CT porosity analysis. The selected specimen was the same specimen monitored during fabrication using infrared thermography and acoustic emission, enabling direct specimen-specific comparison between the in-line monitoring signals and the internal porosity subsequently quantified by micro-CT. This approach was adopted to benchmark the capability of the newly developed combined methodology to detect build anomalies.

2.4 Mechanical testing

Tensile testing was carried out on a quasi-static Instron Universal Testing machine (Instron 3369, Instron Co., Ltd., USA), equipped with a non-contacting video Extensometer AVE2. The crosshead velocity was set to 1 mm/min with a 5 kN load cell. Testing followed BS EN ISO 527-1:2019 [36] testing 3 specimen per process parameter set as seen in Fig. 1d. The mechanical tests have been used as a qualitative correlation tool, to link process-induced degradation in the as-built condition, identified non-destructively through in-line monitoring, with the resulting mechanical response. The reported values therefore serve to confirm observed process–structure–property trends rather than to establish statistically representative material properties.

3 Results and discussion

3.1 In-line monitoring (Infrared thermography)

3.1.1 Line plots

Infrared thermographs obtained from the recordings of the manufacturing process are shown in Fig. 3 and the associated pixel profile plots are shown graphically in Fig. 4. The thermographs show the cube being built vertically from the build platform with the nozzle having completed one deposition along the wall of the cube. The pixel size is 0.2 mm and the images are taken at 60% max build cycle time to target the deposition of the infill as the thermal gradient within the infill can have an effect on the tensile properties and warpage of samples [9]. The colour scale has been adjusted to remove background temperatures and focus on the nozzle and the material.

The expected variation of colour across the deposited layer is higher temperature material on the nozzle on the left side of the sample, and lower temperature material on the right side of the sample in a homogenous cooling curve. The IrT images along with the profile plots show unexpected thermal distribution across the deposited layer across all predefined process parameter sets, deviating from the expected variation. In Fig. 4, the initial peaks in all samples between 0 and 2 mm can be attributed to the nozzle, quantified in Table 2. Therefore, the average temperatures are calculated from the line plot data corresponding to the 2–10 mm length of the deposited part, thereby excluding the initial 0–2 mm region.

Figures 3a and 4a show the Extra Fast sample displaying the largest deviation from the expected near monotonic

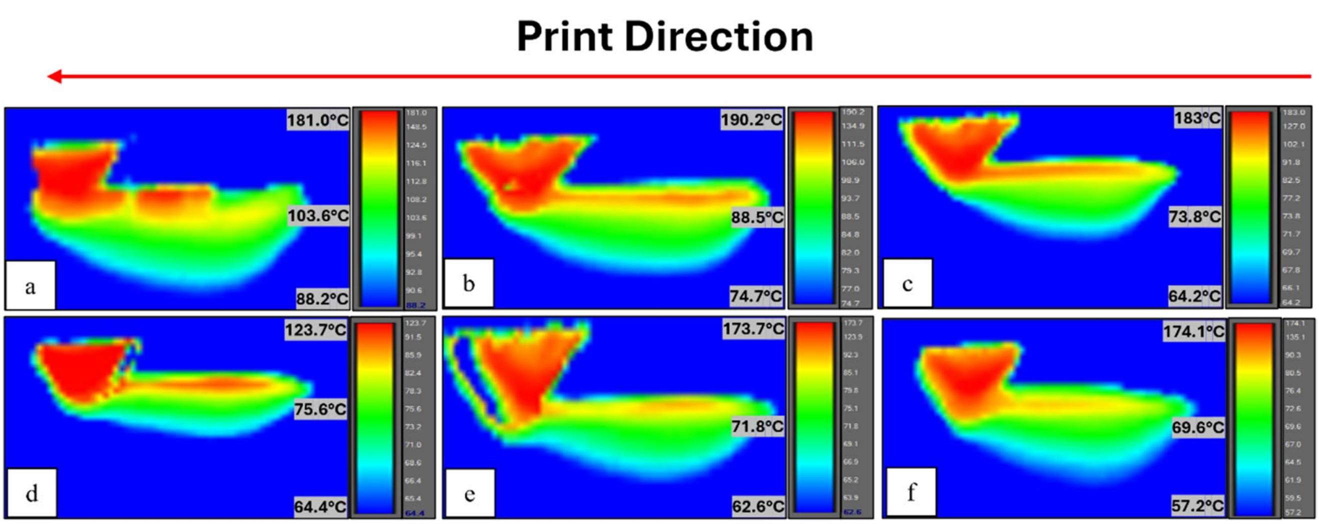

Fig. 3 IrT images **a**) extra fast, **b**) fast, **c**) normal, **d**) fine, **e**) extra fine, **f**) custom

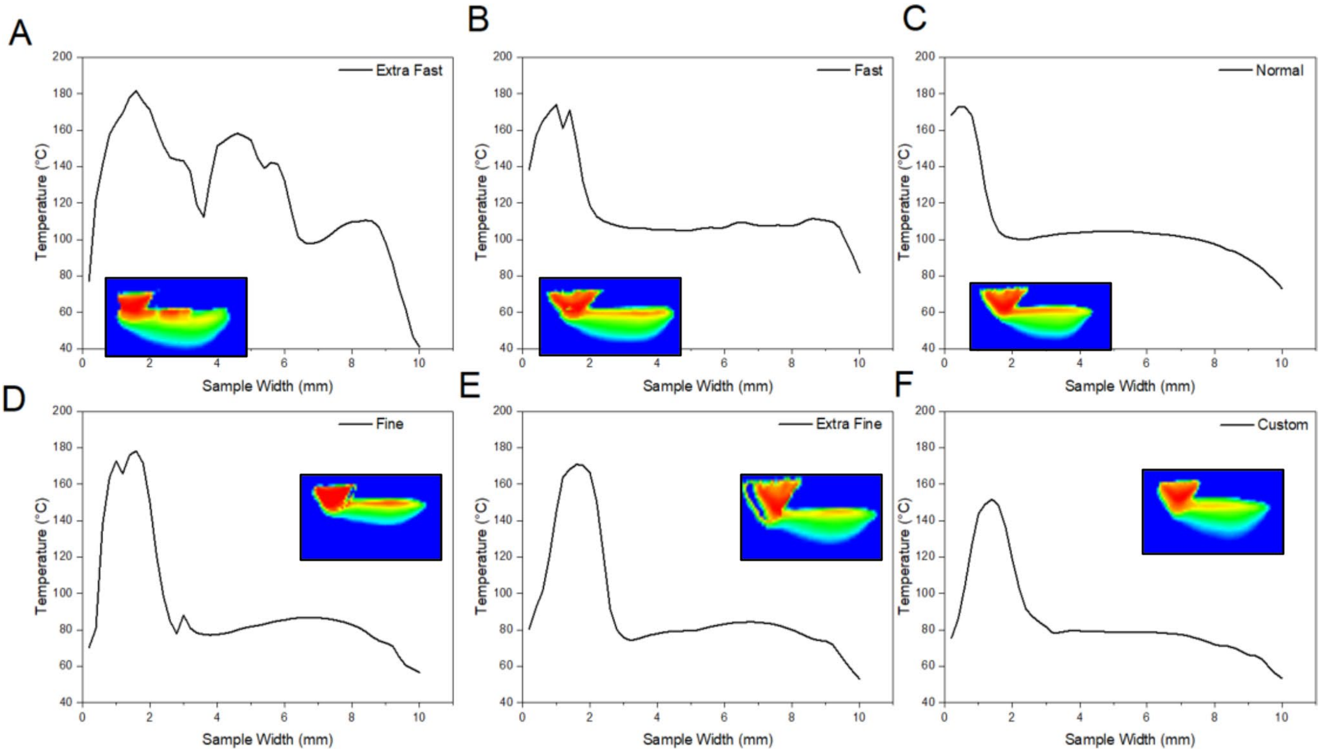

Fig. 4 Pixel profile plots showing the temperature across the process parameter sets (**a**) extra fast, (**b**) fast, (**c**) normal, (**d**) fine, (**e**) extra fine and (**f**) custom

Table 2 IrT profile plot temperature results with standard deviation depicted in brackets

Sample	Extrusion Temperature (°C) (expected)	Average Temperature (°C) (2–10 mm)
Extra Fast	210	119.0 (30.30)
Fast	205	106.3 (5.26)
Normal	200	98.4 (7.89)
Fine	200	80.8 (10.43)
Extra Fine	195	82.5 (6.21)
Custom	195	75.9 (8.72)

cooling behaviour across the deposited road. The material exhibits the widest temperature spread (approximately 40–160 °C) and the highest mean surface temperature (Table 2), together with a pronounced secondary maximum between 4 and 6 mm along the profile. In material extrusion additive manufacturing, interlayer bond formation is governed by the coupled processes of intimate contact, wetting, and time dependent molecular interdiffusion across the interface, all of which are strongly dependent on temperature and time. Experimental studies have demonstrated that diffusion and intimate contact contribute separately to the resulting bond strength, and that sufficient "weld time" above the glass transition temperature (T_g) is a critical requirement for effective interlayer consolidation [42, 43].

In-situ infrared thermography measurements reported in the literature show that, under typical printing conditions, the weld temperature can decay rapidly (on the order of 100 $°C\cdot s^{-1}$) and remain above T_g for only ~ 1 s, which provides a practical benchmark for what constitutes a "sufficient" thermal window for bonding [43, 44]. Accordingly, the elevated temperatures measured in the Extra Fast case are consistent with a thermal state that can promote molecular diffusion. However, the very short build cycle simultaneously reduces the time available for pressure driven consolidation and for the deposited road to stiffen before subsequent layer deposition. This can reduce the effective local contact pressure at the interface, promote geometric instability, and facilitate the formation of entrapped voids. This interpretation is consistent with the systematic and repeatable "crossing pattern" porosity observed in the micro-CT reconstructions (Figs. 9, 10 and 11), indicating a process induced consolidation issue linked to toolpath and thermal history rather than a random thermal artefact.

Figures 3d and 4d show the *Fine* sample with temperatures ranging between 50 and 90 °C and an average temperature of 80.8 °C across the material. The line plot shows a sharp unexpected peak at 3 mm however this is likely caused by a reflection of the nozzle and not the material itself. Figures 3e and 4e show the *Extra Fine* sample with similar cooling behaviour to the *Normal* sample. The temperatures of the extruded material range from 50 to 90 °C with an average of 82.5 °C. Although the overall temperature range is lower, there is a broad but less defined peak between 4 and 8 mm indicating retained heat on the right of the extruded material. There is an improvement in average temperature between the *Normal* and *Extra Fine* with a 16.2% decrease for a 2.4x increase in build cycle time. Figures 3f and 4f show the *Custom* sample with similar cooling behaviour to the *Normal* and *Extra Fine* samples. The temperatures range from 53 to 80 °C with an average temperature of 75.9 °C. There was an improvement in the average temperature between the *Extra Fine* and *Custom* with an 8% decrease for a 1.33x increase in build cycle time. The *Fine*, *Extra Fine*, and *Custom* profiles exhibit lower mean temperatures and reduced spatial variation, suggesting a more stable thermal history that supports more consistent interlayer consolidation and reduced intra layer porosity.

3.1.2 Residual temperature monitoring

Infrared thermographs obtained from the recordings of the manufacturing process are shown in Fig. 5. The pixel size is 0.2 mm and the images are taken at 60% max build cycle time. The boxes seen in Fig. 5 are 50×30 pixels and the information extracted is the average temperatures across the area. This quantity will affect the internal layer structure if proper cooling is not achieved. This trade-off between allowing layers sufficient time to cool versus maintaining sufficient temperature for internal bonding has been difficult to achieve, with attempts made to model the behaviour [46]. The initial peaks in all samples between 0 and 2 mm can be attributed to the nozzle. The average temperatures across the samples are shown in Table 3 and graphically in Fig. 6.

From the predefined process parameter sets, the *Extra Fast* sample exhibited the highest average residual temperature (Table 3), indicating the greatest degree of heat retention within the part during fabrication. Importantly, the part cooling fan speed was maintained constant at 100% across all printing profiles (Sect. 2); therefore, differences in residual temperature primarily reflect the combined effects of layer thickness, building speed, and build cycle time rather than changes in forced convection conditions. In polymer material extrusion processes, higher interfacial temperatures generally promote wetting and molecular diffusion across the layer interface. However, this enhancement is

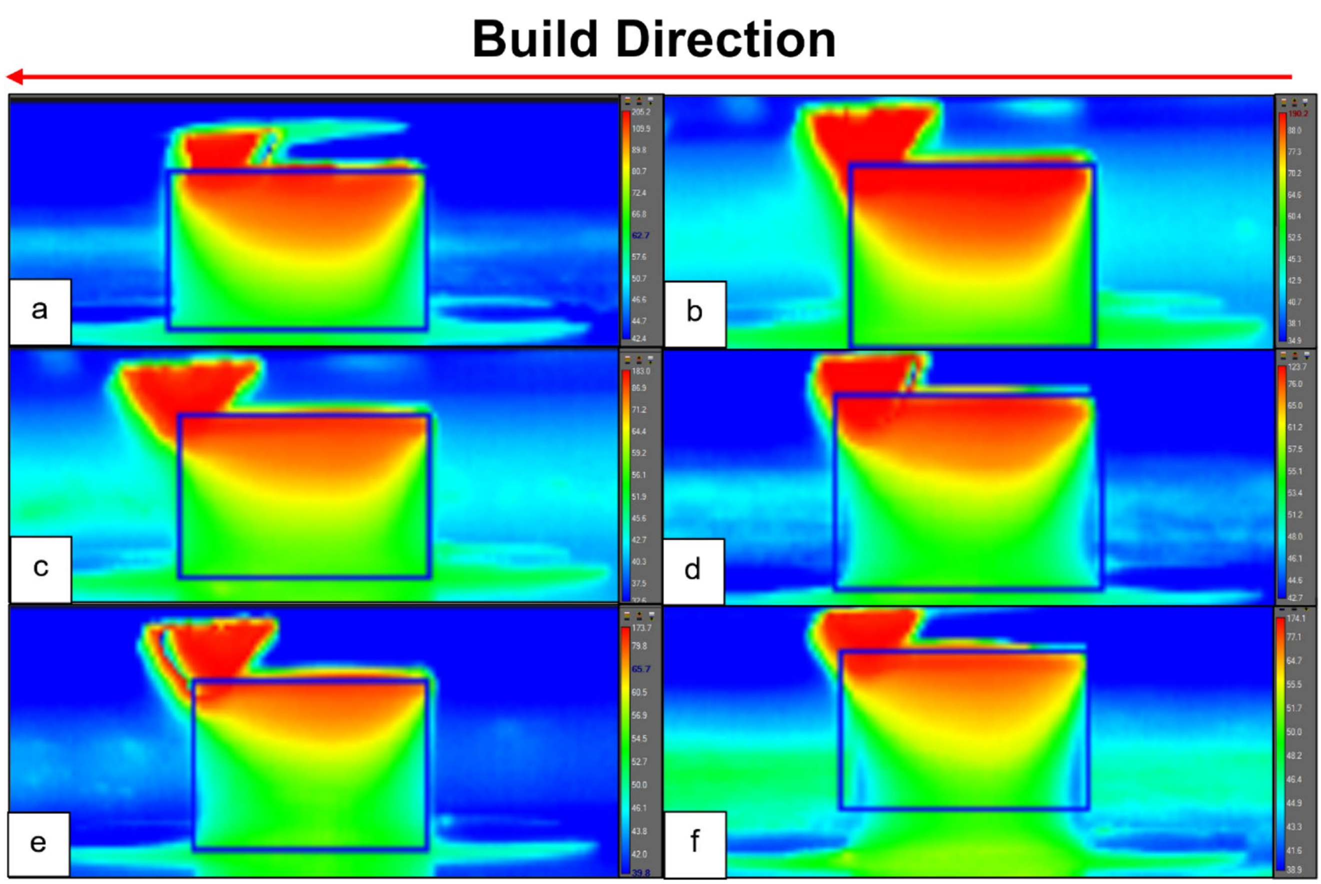

Fig. 5 IrT images of the four cubic samples from the side view orientation with a box plot annotated. (**a**) extra fast, (**b**) fast, (**c**) normal, (**d**) fine, (**e**) extra fine and (**f**) custom

Table 3 Residual temperature monitoring results

Sample	Average Residual Temperature (°C)
Extra Fast	80.90
Fast	76.18
Normal	66.96
Fine	61.40
Extra Fine	58.54
Custom	57.61

only effective when accompanied by sufficient intimate contact and adequate weld time above T_g [43, 45]. Excessive heat retention in the absence of sufficient consolidation time does not inherently lead to poor adhesion; instead, it more commonly manifests reduced dimensional stability, including creep, sagging, and warpage, as well as modified void morphology due to local remelting and viscous flow of previously deposited material [43, 47]. Consequently, in this study, the higher residual temperatures observed in samples are interpreted primarily as a risk factor for geometric instability and repeatable internal void formation, rather than as a direct mechanism for degraded interlayer adhesion. The progressive decrease in residual temperature with decreasing layer thickness and increasing build cycle time is consistent with the line plot thermography results (Sect. 3.1.1) and aligns with the observed reduction in porosity quantified via micro-CT for the slower printing profiles.

Cooling rate and overall thermal history are critical parameters influencing both mesostructure development and interlayer bonding in filament-based material extrusion. Experimental and modelling studies have shown that variations in convection conditions and thermal gradients can significantly alter the cooling profile, mesostructure, and bond quality of build parts [47]. At the layer interface, restoration of mechanical integrity is governed predominantly by time dependent molecular interdiffusion, commonly described using reptation based healing theory, and is preceded by surface approach, wetting, and intimate contact between adjoining filaments [43, 44]. For semi-crystalline polymers such as PLA, crystallization influences stiffness and residual stress development; however, premature crystallization can also restrict polymer chain mobility and thereby hinder molecular interdiffusion. As a result, interlayer bonding should not be attributed to crystallization time alone. Crystallinity and microstructure were not directly measured in the present study. Therefore, the observed variations in temperature and thermal gradients are interpreted as indirect indicators that may influence microstructural development and mechanical response, consistent with trends reported

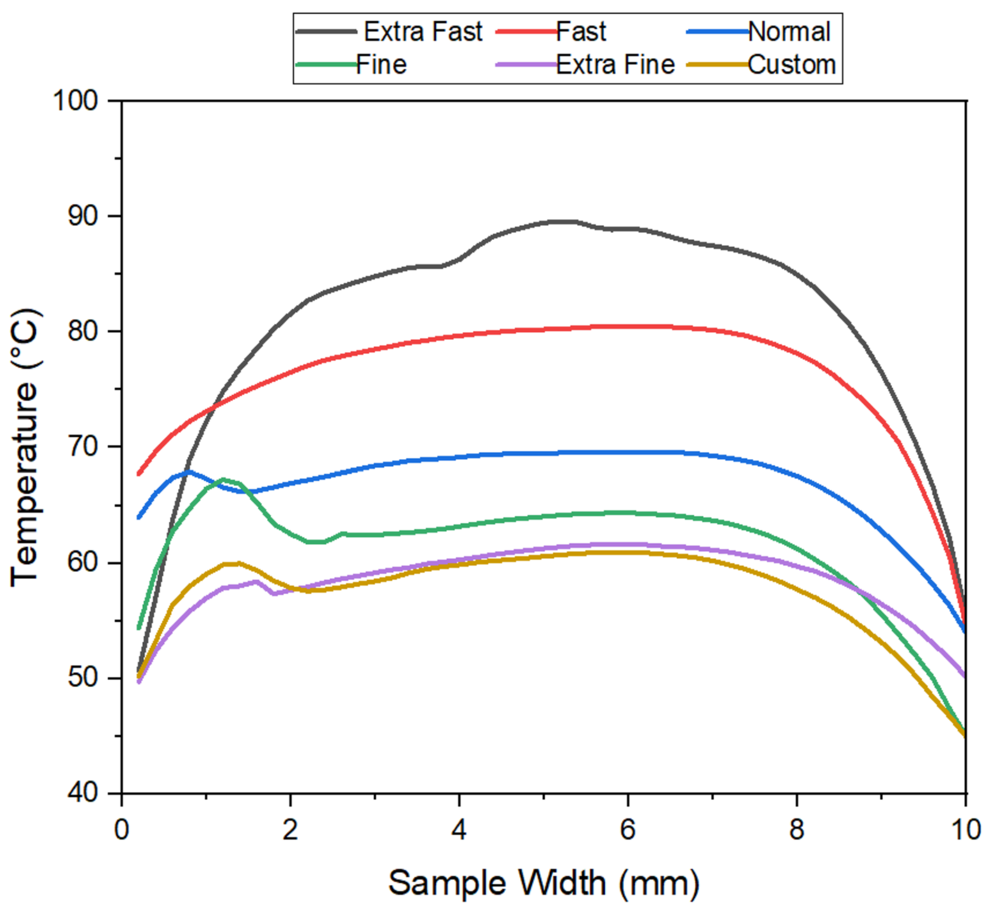

Fig. 6 Pixel box plots showing the average temperature across the extruded material at 60% build cycle time

in the literature. Instead, the residual temperature and local thermal gradients measured in this work serve as proxies for the available weld time above T_g and for the likelihood of thermally induced distortion, both of which can influence the final porosity content and mechanical response of the manufactured samples. Post-process thermal annealing of MEX PLA has been shown to reduce residual stresses and increase crystallinity, often improving stiffness and strength along raster directions, while interlayer strength remains governed by diffusion-controlled bonding [48]. This highlights that both in-situ thermal history and post-process thermal treatment contribute to the final mechanical performance of material extrusion components.

Figure 7 illustrates the thermal progression of the samples following deposition. The *Extra Fast* sample exhibits the largest thermal gradients and the most rapid temperature decay from the freshly deposited road towards the bulk of the part. This behaviour is more interpreted as a reduction in effective weld time above T_g and a corresponding limitation in the time available for polymer chains to reptate and entangle across the interlayer interface before solidification [44, 45]. This interpretation is consistent with infrared thermography studies demonstrating that the critical temperature window for interlayer welding is typically very short (on the order of seconds or less) under standard processing conditions [45].

Table 4 Acoustic emission findings with standard deviation included in brackets where appropriate

Sample	Average Hit/min*layers
Extra Fast	2.906 (0.63)
Fast	1.311 (0.26)
Normal	0.978 (0.33)
Fine	0.458 (0.24)
Extra Fine	0.561 (0.10)
Custom	0.171 (0.08)

3.2 In-line monitoring (Acoustic emission)

In this section, AE results will be presented. Initial raw results of number of hits and time were recorded. In the present configuration, the acoustic emission sensor was mounted on the extruder head, and the recorded acoustic activity is therefore attributed to a combination of process-related sources, including mechanical motion of the deposition system, material flow within the nozzle, and deposition interactions at the nozzle–material interface. These contributions may be further influenced by process instabilities such as irregular extrusion or non-uniform deposition. Due to the nature of the process, there will be regular repeated acoustic events as the extruder head follows its path. The raw results were then processed to normalise for time and number of layers to account for this regular movement and distinguish any outliers. A summary of the acoustic emission findings is listed in Table 4.

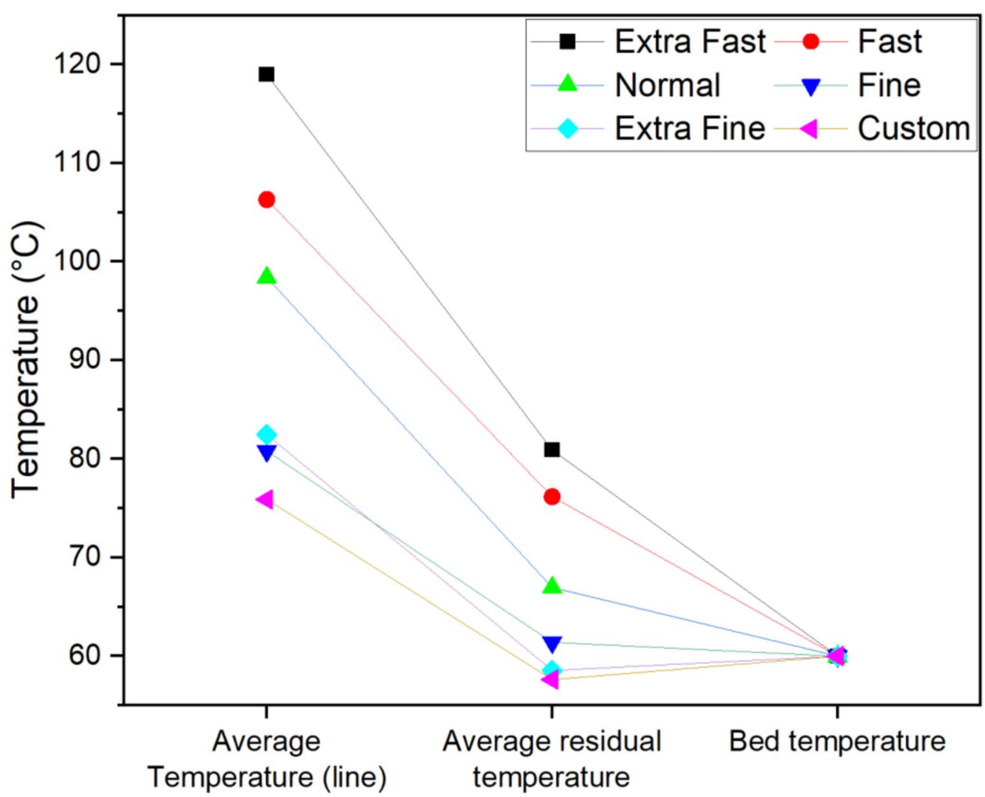

Fig. 7 Thermal progression within samples once manufactured

Once the raw results were normalised to account for build cycle time and number of layers, the *Extra Fast* recorded the most normalised hits on average. This is a 122% increase from the *Fast* sample and a 418% increase from the *Extra Fine* sample, the expected "best" predefined process parameter set. The increased AE activity is consistent with process-induced material phenomena, including non-uniform deposition, poor consolidation and possible local interfacial degradation; however, detailed AE source attribution would require further amplitude- and frequency-domain analysis. This interpretation is supported by: (i) infrared thermography results showing pronounced thermal non-uniformities, high residual temperatures, and steep cooling gradients for the *Extra Fast* profile (Fig. 4a); and (ii) the micro-CT results, which show a higher porosity content and systematic deposition-related void networks, including infill–wall interfacial gaps and regions of limited geometric contact (Figs. 8, 9, 10 and 11). Such features are consistent with localized interfacial degradation rather than purely mechanical noise. A progressive reduction in normalised average hits is observed as the build profiles transition from faster to slower and finer configurations profiles, following the trend of the decrease in average temperature of the material and average residual temperature seen in the IrT results. The *Custom* sample also shows lower normalised average hits. This is concurrent with initial findings for the predefined process parameter sets, where a decrease in layer thickness and increase in build cycle time leads to a decrease in porosity and defects, although this will need to be quantified through the offline assessment.

3.3 Offline assessment – micro-CT scanning

All the samples, once manufactured, were scanned with micro-CT creating a computational reconstruction of the cubes from a series of 2D projection images. The 3D reconstructions will be presented as 2D images, with Fig. 8 showing renderings in CTVox and Fig. 9 showing renderings in CTVol. The images of Fig. 9 have been post-processed through CTAn, for which the porosity has been attempted to be quantified.

Figure 8 shows the volume renders of the cubed samples in CTVox with red areas, as the less dense material, which in this case is air, indicating voids/porosity. The PLA has been removed from Fig. 8 to highlight the porosity present in each build. Figure 8a-f shows 3 d cubic samples with 100% infill. It is expected to be solid, however, this is not the case with MEX, as some amount of porosity is always present (lowering quality), that corresponds mainly to both the process parameters, the nozzle (size and type), and the material itself. Figure 8a shows the *Extra Fast* sample exhibiting a high density of volumetric geometric defects in the form of air gaps and voids, primarily aligned along the wall contours and at the infill–wall interface. These features manifest as systematic deposition-related voids rather than direct indicators of interfacial polymer bonding strength. In material extrusion additive manufacturing, such porosity is typically associated with toolpath planning parameters—such as insufficient infill–wall overlap, limited inter-road contact area, and extrusion instabilities at high deposition speeds—rather than a failure of molecular-scale

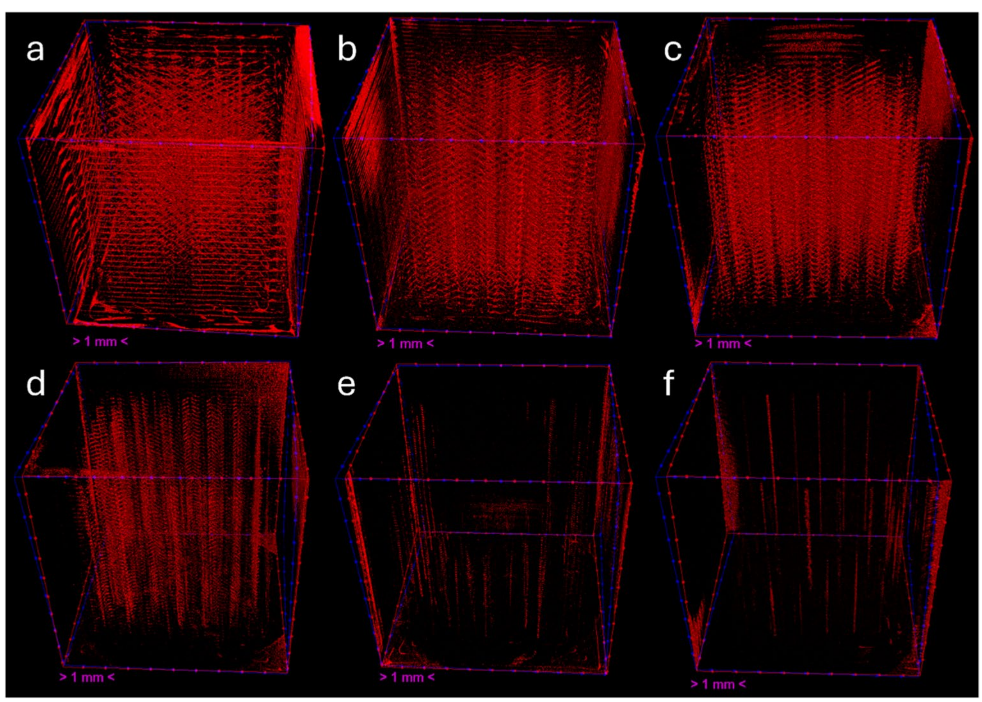

Fig. 8 Micro-CT renderings of all process parameter sets (**a**) extra fast, (**b**) fast, (**c**) normal, (**d**) fine, (**e**) extra fine and (**f**) custom

Fig. 9 CTVol Air renderings for all process parameter sets (**a**) extra fast, (**b**) fast, (**c**) normal, (**d**) fine, (**e**) extra fine and (**f**) custom

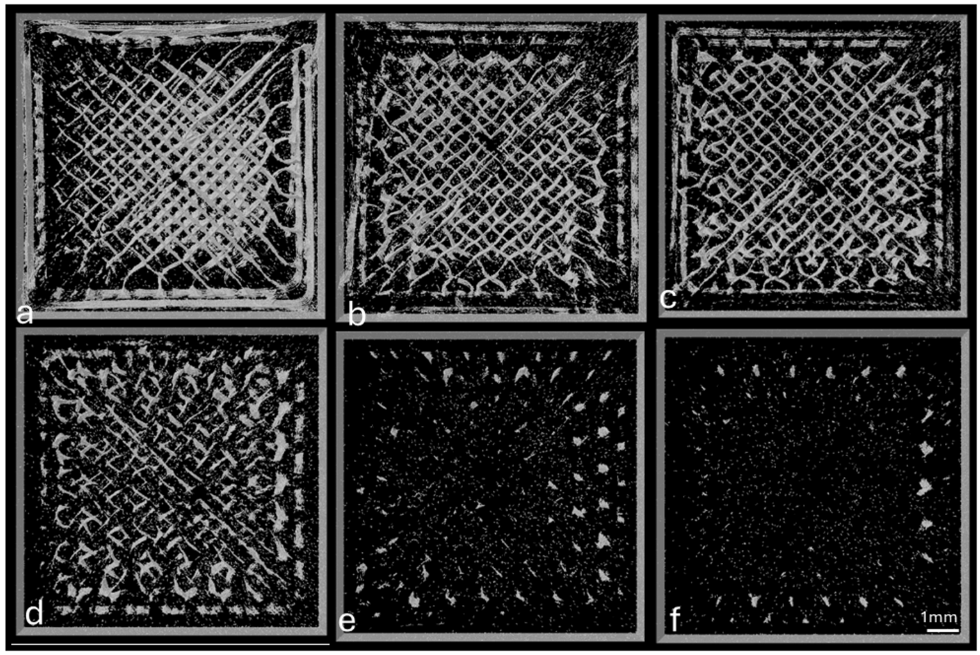

interlayer consolidation. Similar infill-related void patterns are observed in the *Fast* and *Normal* samples, albeit with reduced volume fraction. As layer thickness decreases and build cycle time increases (Figs. 8d–f), the frequency and continuity of these geometric voids are reduced, indicating improved deposition uniformity and infill–wall conformity. While improved thermal conditions, evidenced by infrared thermography, are conducive to enhanced interfacial bonding, the micro-CT results presented here are used strictly to characterise volumetric defect distribution and not as a direct measure of polymer–polymer adhesion quality.

Figure 9 illustrates the internal volume renderings of all the manufactured cubic samples, with the grey colour representing porosity inherently to the samples. Figure 9a depicts

Fig. 10 Quantified porosity percentages for all process parameter sets

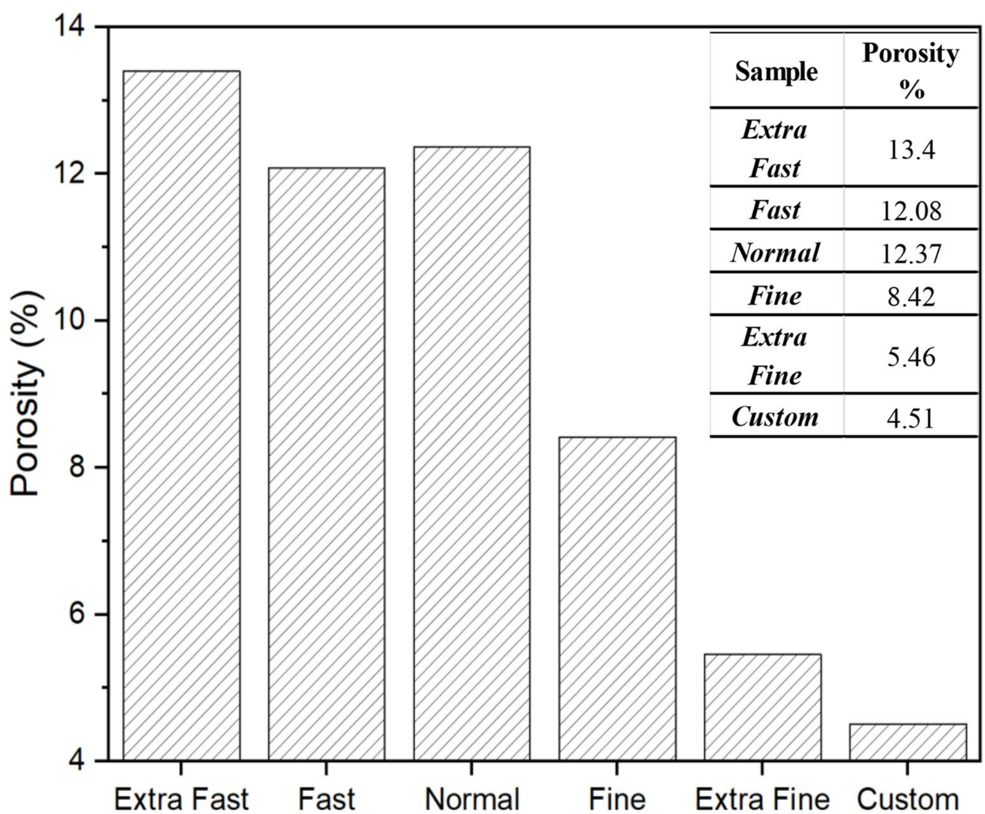

Sample	Porosity %
Extra Fast	13.4
Fast	12.08
Normal	12.37
Fine	8.42
Extra Fine	5.46
Custom	4.51

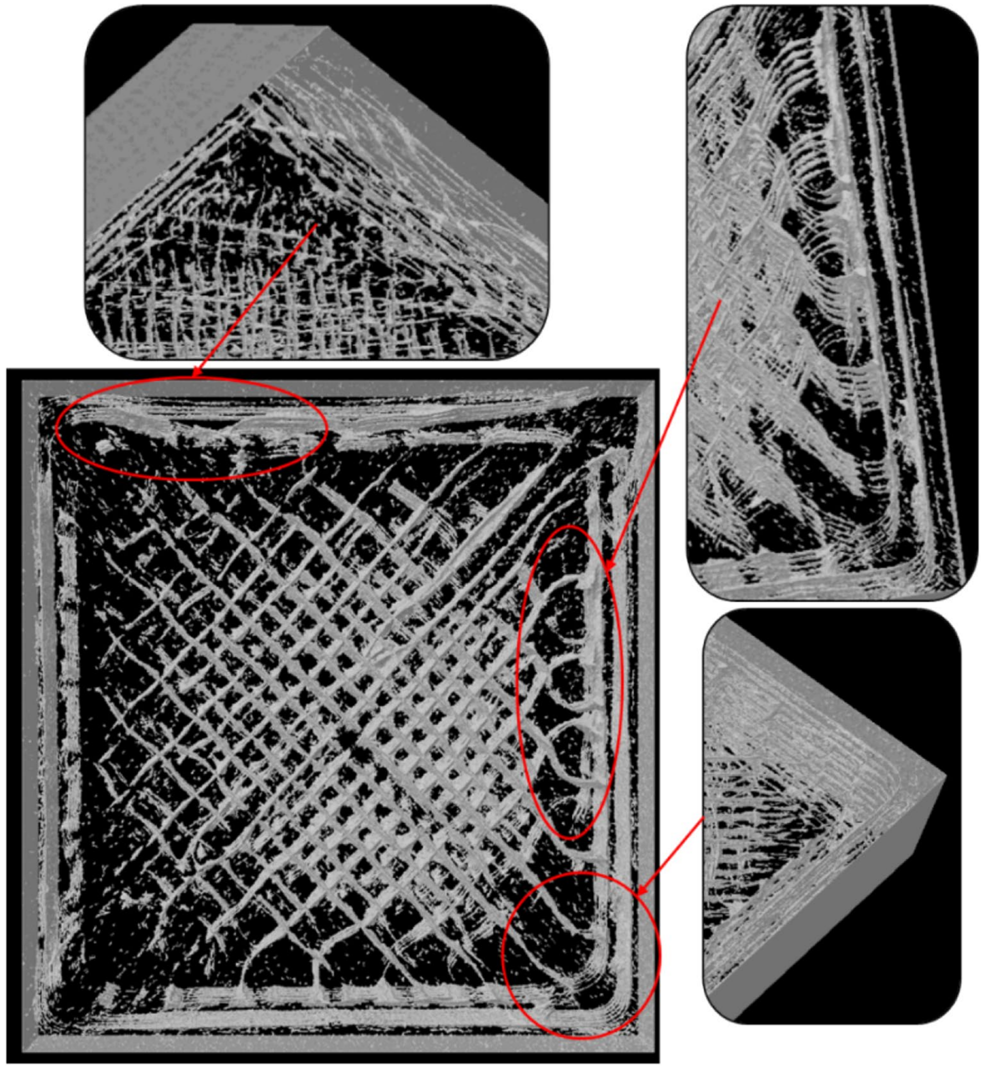

Fig. 11 CTVol Air render for the extra fast (Fig. 9a) showing the multi-layer and repeatable nature of the porosity

the *Extra Fast* with the "crossing pattern" seen in Fig. 8a clearly shown repeatedly across multiple layers, confirming the crossing pattern isn't a unique singular defect, it is systematically repeating on each layer. This is shown in greater detail in Fig. 11, with multiple angles showing the systematic nature of the defects between layers. However, the size/volume of the "crossing pattern" defect does change on each layer which could be caused by different cooling rates, uneven thermal distribution or uneven material deposition. There is also a consistent line of porosity between the inner and outer wall and between the inner wall and the infill. A similar pattern is seen in the *Fast* sample in Fig. 9b, although the porosity between the inner and outer walls is less.

Figure 9c shows the *Normal* cube. Although the "crossing" pattern is still present, the size of the porosity has decreased compared to the *Extra Fast* sample case. The *Fine* sample (Fig. 9d) shows improvement in void content compared to the *Normal*, with a marked decrease in porosity between the inner and outer walls, as well as less connected strings of porosity in the crossing pattern in the infill. The porosity follows similar patterns to the Fig. 9a-c, but the lines are less consistent and connected, with more short voids than long, connected strings of porosity. Figure 9e shows the *Extra Fine* cube where the "crossing pattern" in the infill centre is now negligible. The only air pockets are visible where the infill meets the wall and at corners of the pattern within the infill. The porosity previously seen in the *Normal* and *Extra Fast* cube between the inner and outer wall is not visible within the *Extra Fine* cube. The air pocket visible where the infill meets the wall is consistently present throughout the vertical layers although this is not consistently present on all 4 wall interfaces in this sample. Figure 9f shows the *Custom* cube volume rendering. The crossing pattern seen in the *Extra Fast* and *Normal* cubes is non-existent and there are fewer vertical air pockets compared to the *Extra Fine* cube. Across the vertical layers, there is porosity where the infill meets the wall, however it is less frequent compared to the *Extra Fine* cube. There is also less repeatable porosity between the inner and outer wall layers compared to the *Extra Fine*.

Figure 10 shows the quantified percentage of porosity within each cubes region of interest (ROI). There is a decrease in the quantified porosity percentage between the *Extra Fast* and the *Normal* cubes, decreasing from 13.4% to 12.4%, although the *Fast* breaks the previous defined trend of porosity decreasing as layer thickness decreases.

However, this general trend is still seen throughout the process parameter sets as the quantified porosity decreases generally across the process parameter sets as layer thickness decreases. This change is concurrent with the volume renders in Fig. 9a-c, where all cubes show the "crossing pattern" but the porosity between the inner and outer wall is decreased. The largest difference in porosity percentage of the predefined process parameter sets is seen between the *Normal* and *Extra Fine* cubes decreasing from 12.4% to 5.5%. This value is concurrent with the CTVol volume renders where the *Normal* cube (Fig. 9c) shows the "crossing pattern" porosity within the infill which is not present in the *Extra Fine* cubes (Fig. 9e). There is a small decrease between the *Extra Fine* and *Custom* cubes, decreasing from 5.5% to 4.5%, due to the lack of vertical porosity between the outer and inner walls. Figure 11 clearly shows the systematic nature of the defects between layers, confirming the crossing pattern isn't a unique singular defect, it is systematically repeating on each layer.

3.4 Mechanical and structural assessment

In this section, the dogbone samples have undergone tensile testing, to allow for the determination of the effects of the differing AM process parameter sets on the mechanical properties. The mechanical behaviour of PLA has been widely researched, however there is a wide range of values offered, listed in Table 5. Table 5 presents literature values for tensile strength of AM PLA samples.

The result of the tensile testing is summarised in Table 6. According to BS EN ISO 527-1:2019 [36] the yield strength (σ_y) coincides with the strength (σ_m) as all our tensile test results follow the type 3 stress-strain curves and for simplification we report these values in the text as Yield Strength. We have also reported the strength at break σ_b for completeness. Yield and tensile strength at break values are displayed graphically in Fig. 12.

The *Extra Fine* and *Custom* samples moduli were inside the manufacturers range, and the *Extra Fast* samples were below the manufacturers range. The trend shown in the Yield strength and Tensile strength at break results did not continue for the Young's modulus results, where the *Normal* sample displayed the highest value, although this is outside of the tolerance range expected by the manufactures

Table 5 Additive manufactured PLA materials' tensile strength reference values

	Tensile Strength (MPa)	Reference
PLA 70% infill, 0.25 mm layer height (thickness)	60.0	[49]
PLA 80% infill density	32.9	[50]
PLA, 100% infill density	52.9–62.8	[51]
PLA 100% infill density, 0.2 mm layer height (thickness)	46.5–49.0	[52]
PLA 100% infill density, 0.2 mm layer height (thickness)	46.0–50.0	[53]
PLA 100% infill density	37.7–44.1	[54]

value. For reference, the manufacturer values were recorded from samples using a 0.15 mm layer thickness, which is a comparable process parameter set to the *Normal*. It has been observed that comparing the *Normal* and *Fine* process parameter sets, there is an inconsistency in the Yield strength trend for the *Fine*. There is a slight drop on the Yield strength from 58.3 (2.0) MPa for the *Normal* to 57.2 (2.3) MPa. This slight drop is in the error margin and cannot be considered as statistically significant change.

In general, the values of the mechanical properties of the samples increased across the process parameter sets with the *Extra Fast* samples having the lowest values and the *Custom* sample the highest values. This trend is concurrent with the finding of the Micro-CT analysis, where decreasing the layer thickness and increasing build cycle time decreased the number of defects and voids present in the sample, therefore decreasing the number of stress concentrators within the sample, leading to higher values of mechanical properties.

3.5 General discussion

From the current body of work, the findings of infrared thermography and acoustic emission provide consistent and complementary information regarding the thermal and mechanical state of the material extrusion process during fabrication. As discussed in Sect. 3.1.1 and 3.1.2, IrT revealed spatial non-uniformities in temperature distribution along the deposited material and enabled monitoring of residual heat retained within the part during the build. These thermal measurements characterise spatial temperature non-uniformity and residual heat retention during fabrication. They are interpreted as indicators of the process thermal history and of conditions that may influence weld time, geometric stability, deposition uniformity, and void morphology, rather than as direct evidence of inadequate interlayer adhesion. The AE results exhibited a broadly similar trend to the IrT observations, with lower normalised acoustic activity under the slower and finer process parameter profiles.

Table 6 Summary of the mechanical properties across the process parameter sets, compared with manufacturer data. Values in brackets indicate the standard deviation, while ± denotes the full range of experimental values reported in the manufacturer TDS

Sample	Yield Strength σ_y and Strength σ_m (MPa)	Tensile Strength at Break σ_b (MPa)	Strain at break (%)	Young's modulus (MPa)
Ultimaker PLA [55]	52.5 ± 0.9	45.5 ± 1.1	7.8 ± 1.2	3250.0 ± 119.0
Extra Fast	52.6 (2.4)	49.4 (2.4)	3.0 (0.3)	3116.0 (15.5)
Fast	55.6 (1.9)	51.8 (3.0)	2.7 (0.4)	3409.0 (14.0)
Normal	58.3 (2.0)	53.7 (3.4)	2.9 (0.4)	3462.5 (1.5)
Fine	57.2 (2.3)	53.1 (3.3)	3.6 (1.3)	3389.5 (9.5)
Extra Fine	59.3 (2.1)	54.5 (3.6)	3.3 (0.9)	3327.0 (16.0)
Custom	60.3 (2.1)	56.4 (3.9)	2.5 (0.3)	3348.0 (29.0)

The developed method based on IrT and AE shows strong potential for industrial implementation applications due to the passive approach and non-intrusive nature of both NDE methods. Specifically, multiple AE sensors can be attached to the extruder head and/or feeder capturing any abnormalities of the additive manufacturing process which produce acoustic activity. Furthermore, IrT has been employed for industrial applications [56] and with the addition of multiple thermal cameras a 360° view (excluding the build platform surface) can be monitored.

Together as one combined methodology, they allow for successful identification of the presence of defects which can then be confirmed and quantified through offline assessment. It has been observed that both IrT and AE show strong indications of defects/process anomalies for all the process parameter sets, but they are not very prominent at the custom process parameter set. At the custom-building cycle, the temperature profile does not show high variation, and normalised AE activity is very low which could be also considered a detection threshold for both methodologies. At this stage, the measured AE signals primarily represent baseline process behaviour rather than defect-related anomalies. Nevertheless, the micro-CT investigation proved that this process parameter set has the lowest porosity and very small defects compared to the others. Furthermore, the offline assessment was able to successfully quantify the presence and volume of defects within the samples, allowing for the IrT and AE results to be benchmarked and confirmed.

The results found in this work show that across the investigated process parameter profiles, the cubic specimens generally exhibited lower micro-CT porosity under the slower and finer processing conditions while the manufactured dogbone specimens generally exhibited higher tensile strength. These parallel trends are interpreted as independent qualitative responses to the applied process profiles. Throughout the predefined process parameter sets, there was an overall decrease in porosity percentage of 60% and an increase in Yield strength of 13% for an overall 6x increase in cube build cycle time and 4.14x increase in dogbone build cycle time. This trend continued into the *Custom*, where there was an overall decrease in porosity percentage of 66% and an

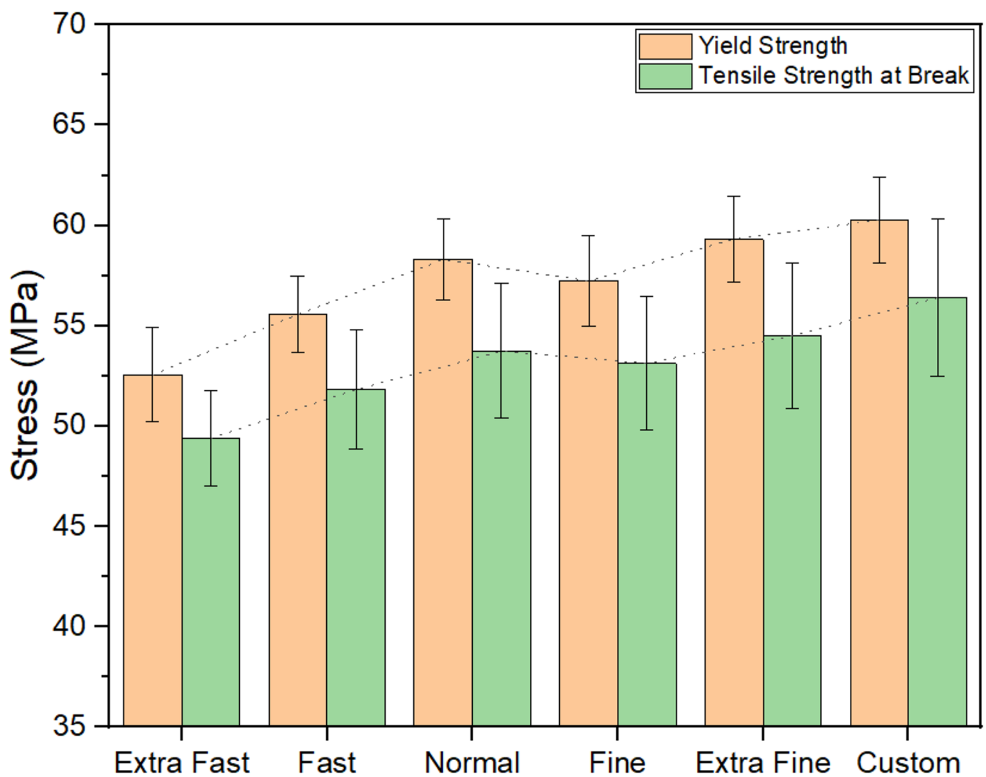

Fig. 12 Average yield strength and tensile strength at break across the manufacturing parameters sets

increase in Yield strength of 15%. Comparatively, this was an 8x and 6.1x increase in overall build cycle time for cubes and dogbones respectively. The nominal volumetric deposition rate decreases from the Extra Fast/Fast conditions towards the Extra Fine/Custom conditions, reflecting the combined reduction in layer thickness and increase in build cycle time. This reduction in material throughput is consistent with the lower residual temperatures, reduced AE activity and lower micro-CT porosity measured for the slower/finer process parameter sets.

Figure 13 shows a trend summary between process parameter sets, mechanical properties as well as the trends in void content. The *Extra Fast* process parameter set has consistently performed the worst when considering porosity percentage and mechanical properties. The *Extra Fast* process parameter set would therefore not produce samples fit for structural applications, however where parts with less structural needs are required, such as prototypes or design models, the reduced build cycle time could be advantageous. Although it is essential to allow the layers sufficient time to cool before the next deposition, allowing too long could have adverse effects, therefore this work presents a wide scope of results to allow for the selection of the properties most suited to the application. When considering structural applications, the *Extra Fine* process parameter set presented as the best option with the benefits of reduced build cycle time outweighing the very small increase in mechanical properties compared to the *Custom*. The results showed a 46% decrease in porosity percentage compared to the *Fine* process parameter set, and a 5.4% and 6.2% increase in Yield Strength and Tensile strength respectively. Although the *Custom* process parameter set did also perform well structurally, for a 46% increase in tensile test specimen build cycle time, it only returned a 1.6% increase in Yield strength and 3.5% increase in Tensile strength at break compared to the *Extra Fine*. Dependent on the requirements, a trade-off could be made here between the build cycle time and mechanical properties, as all samples but the *Extra Fast* exceeded the manufacturer results in both Yield Strength and Young's Modulus.

4 Conclusions

In the present work, a combination of NDE techniques is employed to detect and assess defects created during the additive manufacturing process. PLA was used to produce both cubed and tensile test samples across different process parameter sets. The proposed monitoring approach, based on in-situ data acquisition using infrared thermography and acoustic emission, enabled the identification of process signatures

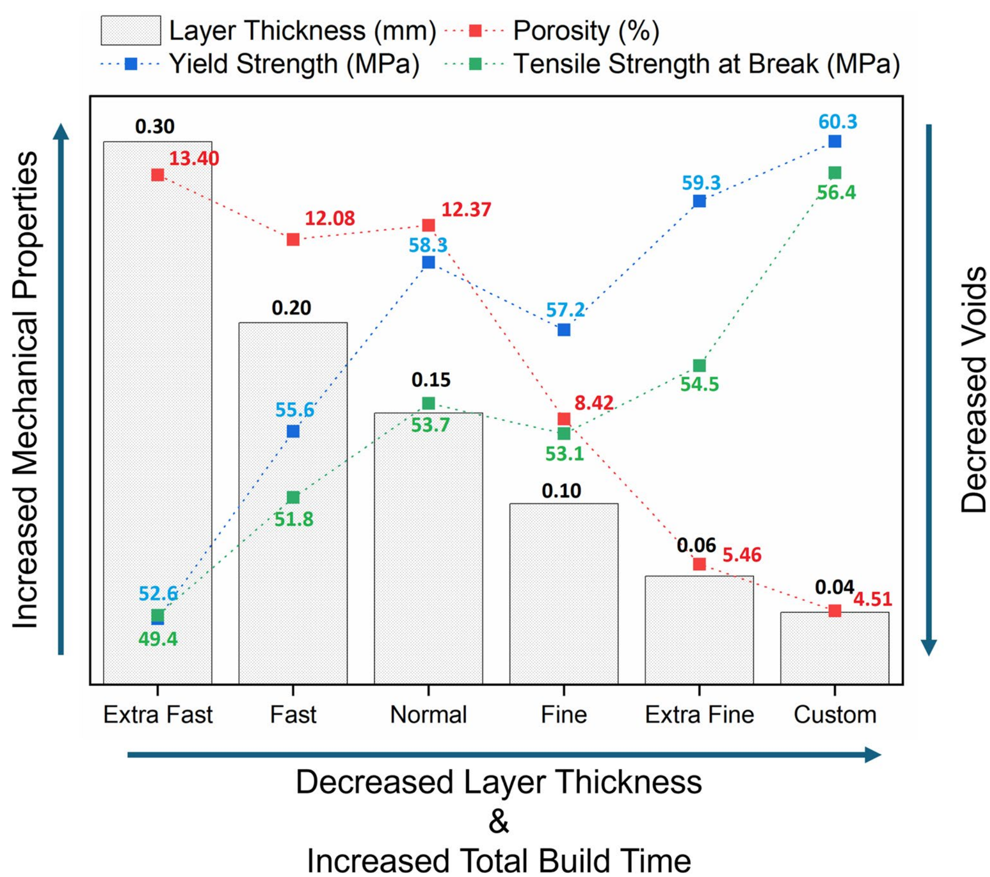

Fig. 13 Schematic/trend summary between process parameter sets, porosity and mechanical properties

associated with anomalies during the fabrication stage. The interpretation of these signals was performed post-process. The samples were then scanned using micro-computed tomography, and the presence and distribution of defects identified in the cubic specimens were found to be consistent with the trends observed in the monitoring data. The mechanical properties were assessed using tensile specimens fabricated under the same process parameter sets; however, due to the differences in specimen geometry and associated thermal histories, the relationship between monitoring data and mechanical performance is interpreted qualitatively in terms of process–structure–property trends rather than as a direct causal correlation.

The monitoring system acquired thermal and acoustic signals during the build process, which, upon post-process analysis, revealed abnormalities such as non-uniform thermal distribution and irregular deposition patterns. The findings from the IrT and AE have been benchmarked against the micro-CT's findings. The micro-CT's results have revealed a decrease in voids and porosity in relation to the layer thickness decrease, with a 59% overall reduction in porosity across the predefined process parameter sets which led to increased mechanical properties. The developed methodology was found to be an effective tool for the monitoring of the MEX additive manufacturing process for the early identification of defects and manufacturing abnormalities demonstrating potential for application in industrial environments, subject to further development of real-time processing capabilities and geometry-specific validation.

Supplementary Information The online version contains supplementary material available at https://doi.org/10.1007/s00170-026-19170-7.

Authors' contributions **Rosanna Forster**: Methodology, Writing – Original Draft, Writing – Review and Editing, Investigation, Formal Analysis, Visualisation, Project Administration. **Evangelos Kordatos**: Conceptualization, Methodology, Writing – Review and Editing, Supervision, Project Administration, Funding acquisition. **Dimitra Soulioti**: Writing – Review and Editing, Supervision, Project Administration. **Antonio Feteira**: Writing – Review and Editing, Supervision. **Sotirios Grammatikos**: Supervision - Review and Editing.
For the purpose of open access, the author has applied a Creative Commons Attribution (CC BY) licence to any Author Accepted Manuscript version arising from this submission.

Funding This research was funded by the Sheffield Hallam University under the "Graduate Teaching Assistant Scheme".

Data availability The data and materials that support the findings of this study are available from the corresponding author upon reasonable request.

Declarations

Competing interests The authors have no relevant financial or non-financial interests to disclose.

References

1. (2021) Terminology for Additive Manufacturing - General Principles - Terminology ASTM ISO/ASTM52900-15. ASTM International, West Conshohocken, PA
2. Gao W, Zhang Y, Ramanujan D et al (2015) The status, challenges, and future of additive manufacturing in engineering. Comput Aided Des 69:65–89. https://doi.org/10.1016/j.cad.2015.04.001
3. Vora HD, Sanyal S (2020) A comprehensive review: metrology in additive manufacturing and 3D printing technology. Progress Additive Manuf 5:319–353. https://doi.org/10.1007/s40964-020-00142-6
4. Fu Y, Downey A, Yuan L et al (2021) In situ monitoring for fused filament fabrication process: A review. Addit Manuf 38:101749. https://doi.org/10.1016/j.addma.2020.101749
5. Chua CK, Leong KF, Lim CS (2010) Rapid Prototyping, Principles and Applications. Assembly Autom 30. https://doi.org/10.1108/aa.2010.03330dae.001
6. Taufik M, Jain PK (2016) A Study of Build Edge Profile for Prediction of Surface Roughness in Fused Deposition Modeling. J Manuf Sci Eng 138:K. https://doi.org/10.1115/1.4032193
7. Krishnanand TM (2025) Surface roughness investigation of 3D printed parts via in-situ pellet-filament co-extrusion process. Mater Manuf Processes 40:1029–1048. https://doi.org/10.1080/10426914.2025.2487275
8. Armillotta A (2019) Simulation of edge quality in fused deposition modeling. Rapid Prototyp J 25:541–554. https://doi.org/10.1108/RPJ-06-2018-0151
9. Croccolo D, De Agostinis M, Fini S et al (2024) Effects of infill temperature on the tensile properties and warping of 3D-printed polylactic acid. Prog Addit Manuf 9:919–934. https://doi.org/10.1007/s40964-023-00492-x
10. Tang C-L, Seeger S, Röllig M (2023) Improving the comparability of FFF-3D printing emission data by adjustment of the set extruder temperature. Atmos Environ X 18:100217. https://doi.org/10.1016/j.aeaoa.2023.100217
11. Anderegg DA, Bryant HA, Ruffin DC et al (2019) In-situ monitoring of polymer flow temperature and pressure in extrusion based additive manufacturing. Addit Manuf 26:76–83. https://doi.org/10.1016/j.addma.2019.01.002
12. Onwubolu GC, Rayegani F (2014) Characterization and Optimization of Mechanical Properties of ABS Parts Manufactured by the Fused Deposition Modelling Process. Int J Manuf Eng 2014:1–13. https://doi.org/10.1155/2014/598531
13. Nath SD, Nilufar S (2020) An Overview of Additive Manufacturing of Polymers and Associated Composites. Polym (Basel) 12:2719. https://doi.org/10.3390/polym12112719
14. Jin Z, Zhang Z, Ott J, Gu GX (2021) Precise localization and semantic segmentation detection of printing conditions in fused

filament fabrication technologies using machine learning. Addit Manuf 37:101696. https://doi.org/10.1016/j.addma.2020.101696
15. Wu H, Yu Z, Wang Y (2019) Experimental study of the process failure diagnosis in additive manufacturing based on acoustic emission. Measurement 136:445–453. https://doi.org/10.1016/j.measurement.2018.12.067
16. Rao PK, Liu J, Roberson D et al (2015) Online real-time quality monitoring in additive manufacturing processes using heterogeneous sensors. J Manuf Sci Eng. https://doi.org/10.1115/1.4029823
17. Zhang J, Wang P, Gao RX (2018) Modeling of Layer-wise Additive Manufacturing for Part Quality Prediction. Procedia Manuf 16:155–162. https://doi.org/10.1016/j.promfg.2018.10.165
18. Smith T, Failla J, Lindahl J et al (2018) Structural Health Monitoring of 3D Printed Structures. In: 29th Annual International Solid Freeform Fabrication Symposium. University of Texas at Austin
19. Akmal Zia A, Tian X, Jawad Ahmad M et al (2023) Impact Resistance of 3D-Printed Continuous Hybrid Fiber-Reinforced Composites. Polym (Basel) 15:4209. https://doi.org/10.3390/polym15214209
20. Ghafoor S, Wang M, Li X et al (2026) Microstructure-guided optimization of octahedral lattice structures for enhanced energy absorption via LPBF. Progress Additive Manuf 11:411–428. https://doi.org/10.1007/s40964-025-01356-2
21. Ghafoor S, Wang M, Li X et al (2026) Integrating microstructural defect mapping into geometric refinement of LPBF lattices for enhanced mechanical performance. J Manuf Process 162:81–98. https://doi.org/10.1016/j.jmapro.2026.02.015
22. Goh GD, Hamzah NM, Bin, Yeong WY (2023) Anomaly Detection in Fused Filament Fabrication Using Machine Learning. 3D Print Addit Manuf 10:428–437. https://doi.org/10.1089/3dp.2021.0231
23. Chen RK, Lo TT, Chen L, Shih AJ (2015) Nano-CT Characterization of Structural Voids and Air Bubbles in Fused Deposition Modeling for Additive Manufacturing. Volume 1: Processing. American Society of Mechanical Engineers, Charlotte, North Carolina, USA
24. Kio OJ, Yuan J, Brooks AJ et al (2018) Non-destructive evaluation of additively manufactured polymer objects using X-ray interferometry. Addit Manuf 24:364–372. https://doi.org/10.1016/j.addma.2018.04.014
25. Zekavat AR, Jansson A, Larsson J, Pejryd L (2019) Investigating the effect of fabrication temperature on mechanical properties of fused deposition modeling parts using X-ray computed tomography. Int J Adv Manuf Technol 100:287–296. https://doi.org/10.1007/s00170-018-2664-8
26. Kattinger J, Kornely M, Ehrler J et al (2023) Analysis of melting and flow in the hot-end of a material extrusion 3D printer using X-ray computed tomography. Addit Manuf 76:103762. https://doi.org/10.1016/j.addma.2023.103762
27. Meshkizadeh P, Hajideh MR, Farahani M, Heidari-Rarani M (2021) Thermal signal reconstruction and employment of K clustering method for inspection of additive manufactured polymer parts. Nondestructive Test Technol 2:60–69
28. Olowe M, Ogunsanya M, Best B et al (2024) Spectral features analysis for print quality prediction in additive manufacturing: an acoustics-based approach. Sensors (Basel) 24:4864. https://doi.org/10.3390/s24154864
29. D'Accardi E, Chiappini F, Giannasi A et al (2024) Online monitoring of direct laser metal deposition process by means of infrared thermography. Progress Additive Manuf 9:983–1001. https://doi.org/10.1007/s40964-023-00496-7
30. Farea SM, Javidrad H, Unel M, Koc B (2026) In-situ defect detection in directed energy deposition using thermal imaging and machine learning. Progress Additive Manuf 11:521–541. https://doi.org/10.1007/s40964-025-01362-4
31. AbouelNour Y, Gupta N (2023) Assisted defect detection by in-process monitoring of additive manufacturing using optical imaging and infrared thermography. Addit Manuf 67:103483. https://doi.org/10.1016/j.addma.2023.103483
32. Bauriedel N, Albuquerque RQ, Utz J et al (2024) Monitoring of fused filament fabrication: An infrared imaging and machine learning approach. J Polym Sci 62:5633–5641. https://doi.org/10.1002/pol.20240586
33. AbouelNour Y, Gupta N (2022) In-situ monitoring of sub-surface and internal defects in additive manufacturing: A review. Mater Des 222:111063. https://doi.org/10.1016/j.matdes.2022.111063
34. Raj SA, Muthukumaran E, Jayakrishna K (2018) A Case Study of 3D Printed PLA and Its Mechanical Properties. Mater Today Proc 5:11219–11226. https://doi.org/10.1016/j.matpr.2018.01.146
35. Kristiawan RB, Imaduddin F, Ariawan D et al (2021) A review on the fused deposition modeling (FDM) 3D printing: Filament processing, materials, and printing parameters. Open Eng 11:639–649. https://doi.org/10.1515/eng-2021-0063
36. (2019) Plastics Determination of tensile properties BS EN ISO 527-1:2019. BSI British Standards, London
37. Frunzaverde D, Cojocaru V, Bacescu N et al (2023) The Influence of the Layer Height and the Filament Color on the Dimensional Accuracy and the Tensile Strength of FDM-Printed PLA Specimens. Polym (Basel) 15:2377. https://doi.org/10.3390/polym15102377
38. Jain R, Nauriyal S, Gupta V, Khas KS (2021) Effects of Process Parameters on Surface Roughness, Dimensional Accuracy and Printing Time in 3D Printing. In: Advances in Production and Industrial Engineering. pp 187–197
39. Butt J, Bhaskar R, Mohaghegh V (2022) Analysing the effects of layer heights and line widths on FFF-printed thermoplastics. Int J Adv Manuf Technol 121:7383–7411. https://doi.org/10.1007/s00170-022-09810-z
40. Serdeczny MP, Comminal R, Pedersen DB, Spangenberg J (2020) Experimental and analytical study of the polymer melt flow through the hot-end in material extrusion additive manufacturing. Addit Manuf 32:100997. https://doi.org/10.1016/j.addma.2019.100997
41. Morgan R, Reid R, Baker A et al (2017) Emissivity Measurements of Additively Manufactured Materials. Los Alamos, NM (United States)
42. (2017) Guide for Mounting Piezoelectric Acoustic Emission Sensors ASTM E650/E650M. ASTM International, West Conshohocken, PA
43. Sun Q, Rizvi GM, Bellehumeur CT, Gu P (2008) Effect of processing conditions on the bonding quality of FDM polymer filaments. Rapid Prototyp J 14:72–80. https://doi.org/10.1108/13552540810862028
44. Seppala JE, Migler KD (2016) Infrared thermography of welding zones produced by polymer extrusion additive manufacturing. Addit Manuf 12:71–76. https://doi.org/10.1016/j.addma.2016.06.007
45. Bellehumeur C, Li L, Sun Q, Gu P (2004) Modeling of bond formation between polymer filaments in the fused deposition modeling process. J Manuf Process 6:170–178. https://doi.org/10.1016/S1526-6125(04)70071-7
46. Choo K, Friedrich B, Daugherty T et al (2019) Heat retention modeling of large area additive manufacturing. Addit Manuf 28:325–332. https://doi.org/10.1016/j.addma.2019.04.014
47. Coogan TJ, Kazmer DO (2017) Bond and part strength in fused deposition modeling. Rapid Prototyp J 23:414–422. https://doi.org/10.1108/RPJ-03-2016-0050
48. Yalkin HE, Ozkan AN (2026) Investigation of Crystal Structure Change and Mechanical Properties of 3D Printed PLA After Annealing. Polym Eng Sci. https://doi.org/10.1002/pen.70551
49. Atakok G, Kam M, Koc HB (2022) Tensile, three-point bending and impact strength of 3D printed parts using PLA and recycled

PLA filaments: A statistical investigation. J Mater Res Technol 18:1542–1554. https://doi.org/10.1016/j.jmrt.2022.03.013
50. Subramaniam SR, Samykano M, Selvamani SK et al (2019) Preliminary investigations of polylactic acid (PLA) properties. p 020038. https://doi.org/10.1063/1.5085981
51. Hodžić D, Pandžić A, Hajro I, Tasić P (2020) Strength Comparison of FDM 3D Printed PLA Made by Different Manufacturers. TEM J 9:966–970. https://doi.org/10.18421/TEM93-18
52. Bakar AABA, Zainuddin MZB, Adam ANB et al (2022) The study of mechanical properties of poly(lactic) acid PLA-based 3D printed filament under temperature and environmental conditions. Mater Today Proc 67:652–658. https://doi.org/10.1016/j.matpr.2022.06.198
53. Lendvai L, Fekete I (2020) Preparation and characterization of poly(lactic acid)/boehmite alumina composites for additive manufacturing. IOP Conf Ser Mater Sci Eng 903:012057. https://doi.org/10.1088/1757-899X/903/1/012057
54. Salem H, Abouchadi H, Elbikri K (2022) PLA Mechanical Performance Before and After 3D Printing. Int J Adv Comput Sci Appl 13:324
55. (2022) Ultimaker PLA TDS
56. Joffre T, Fauny G, Runacher A et al (2024) Innovative composite structures by combining ATL and FFF processes. In: European Conference on Spacecraft Structures, Materials and Environmental Testing